Materials Horizons

# A skeletal randomization strategy for high-performance quinoidal-aromatic polymers



| | |
|---|---|
| Journal: | *Materials Horizons* |
| Manuscript ID | MH-COM-07-2023-001143.R1 |
| Article Type: | Communication |
| Date Submitted by the Author: | 17-Oct-2023 |





| | |
|---|---|
| Complete List of Authors: | Zhou, Quanfeng; Guizhou University<br>Liu, Cheng; Guizhou University<br>Li, Jinlun; Guizhou University<br>Xie, Runze; Guizhou University<br>Zhang, Guoxiang; Guizhou University<br>Ge, Xiang; Guizhou University, College of Mateirals and Metallurgy<br>Zhang, Zesheng; South China University of Technology Institute of Polymer Optoelectronic Materials and Devices<br>Zhang, Lianjie; South China University of Technology Institute of Polymer Optoelectronic Materials and Devices,<br>Chen, Junwu; South China University of Technology, Institute of Polymer Optoelectronic Materials and Devices<br>Gong, Xiu; Guizhou University, College of Physics<br>Yang, Chen; Guizhou University<br>Wang, Yuanyu; Guizhou University,<br>Liu, Yi; Lawrence Berkeley Laboratory, Molecular Foundry<br>Liu, Xuncheng; Guizhou University, |
| | |

# New Concepts

This paper introduces an innovative concept in the design of high mobility conjugated polymer research, challenging the conventionally perceived trade-off between solubility and crystallinity that has long constrained the practicality of conjugated polymers. Our study disrupts this dichotomy with the successful application of a skeletal randomization approach. By introducing randomized sequences in a quinoid-aromatic polymer system, a fine balance between solubility and interchain aggregation strength was achieved, leading to enhanced solubility, increased crystallinity, and a much higher carrier transport mobility compared to its regioregular counterparts. Our method offers a remarkable divergence from traditional solubility-tuning methods by simultaneously fostering solubility and thin-film crystallinity. In a counterintuitive fashion, the introduced "disorder" along the backbone has resulted in notably improved film crystallinity and a hole mobility of 3.11 $cm^2 V^{-1} s^{-1}$, 50-times higher than the regioregular homologues. This also places the resulting polymer among the highest performing quinoidal CPs, which additionally demonstrating superior solution-processibility and device stability. The insights provided by our work presents a ground-breaking departure from established norms, illuminating a novel path for designing solution processed high performing conjugated polymers that may find wider applications in organic electronics.

# A skeletal randomization strategy for high-performance quinoidal-aromatic polymers

*Quanfeng Zhou,[†,‡] Cheng Liu,[†,‡] Jinlun Li,[†,‡] Runze Xie,[†] Guoxiang Zhang,[†] Xiang Ge,[†] Zesheng Zhang,[#] Lianjie Zhang,[#] Junwu Chen,[#] Xiu Gong,[$] Chen Yang,[£] Yuanyu Wang,[†,*] Yi Liu[&,§,*] and Xuncheng Liu[†,*]*

[†]College of Materials and Metallurgy, [$]College of Physics and [£]College of Big Data and Information Engineering, Guizhou University, Guiyang 550025, China

[&]The Molecular Foundry and [§]Materials Sciences Division, Lawrence Berkeley National Laboratory, One Cyclotron Road, Berkeley, California, 94720, USA

[#]Institute of Polymer Optoelectronic Materials and Devices, State Key Laboratory of Luminescent Materials and Devices, South China University of Technology, Guangzhou 510640, China

[‡]These authors contributed equally

**Abstract:** Enhancing the solution-processability of conjugated polymers (CPs) without diminishing their thin-film crystallinity is crucial for optimizing charge transport in organic field-effect transistors (OFETs). However, this presents a classic "Goldilocks zone" dilemma, as conventional solubility-tuning methods for CPs typically yield an inverse correlation between solubility and crystallinity. To address this fundamental issue, a straightforward skeletal randomization strategy is implemented to construct a quinoid-donor conjugated polymer, PA4T-Ra, that contains para-azaquinodimethane (*p*-AQM) and oligothiophenes as the repeat units. A systematic study is conducted to contrast its properties against polymer homologues constructed following conventional solubility-tuning strategies. An unusually concurrent improvement of solubility and crystallinity is realized in the random polymer PA4T-Ra, which shows moderate polymer chain aggregation, highest crystallinity and least lattice disorder. Consequently, PA4T-Ra-based OFETs, fabricated under ambient air conditions, deliver an excellent hole mobility of 3.11 $cm^2 V^{-1} s^{-1}$, which is about 30-times higher than that of the other homologues and ranks among the highest for quinoidal CPs. These findings debunk the prevalent assumption that a random polymer backbone sequence results in decreased crystallinity. The considerable advantages of the skeletal randomization strategy illuminate new possibilities for the control of polymer aggregation and future design of high-performance CPs, potentially accelerating the development and commercialization of organic electronics.

## 1. Introduction

The pursuit of high-performing conjugated polymers (CPs) has been central for the advancement of organic solar cells (OSCs),[1-3] organic field-effect transistors (OFETs)[4-6] and other electronic devices.[7-9] Recently, OFETs have shown promising potential in their use as driving circuits for large-area flexible displays and other types of flexible electronics, the performance of which is largely determined by the CPs utilized in the active layer.[10-12] Understanding the correlation between molecular structure and material property in high mobility CPs is critical to empower the design of CPs with enhanced performance.[13]

Structural design of CPs involves careful consideration of the conjugated structure of the repeat unit, the number of the repeat unit (i.e., molecular weight), and the structure and density of sidechains. Typically, the conjugation of repeat unit is deterministic to intrinsic optoelectronic properties of CPs, while the molecular weight[14, 15] and alkyl sidechains[16-18] can be tailored to incur sufficient solubility in organic solvents. This solubility facilitates necessary solution-processibility for the fabrication of high performance thin-film OFET devices.[17, 19] However, sidechain engineering can substantially affect interchain interactions and self-assembly of CPs, compromising film crystallinity and charge carrier transport in devices,[18, 20 21, 22] not to mention the increased synthetic complexity towards controlling the structure and density of side chains and the polymerization conditions.[23] This balance between solubility, film morphology and carrier mobility presents one of the fundamental challenges for developing high mobility CPs. Therefore, novel solubility-tuning strategies that simultaneously enhance solubility and ordered molecular packing, thereby boosting carrier mobility, are in high demand for achieving high-performance OFETs. [24, 25]

Mixed quinoidal-aromatic CPs containing quinoidal units in the conjugated polymer backbone have exhibited distinctive optoelectronic properties and impressive semiconducting properties, inspiring complementary design principles to the classic donor-acceptor (D-A) type CPs.[26-28] The introduction of a quinoidal unit with oligothiophene in the repeat unit in the polymer backbone often leads to high mobility due to reinforced backbone, strong interchain interaction and aggregation, high crystallinity, and dense molecular packing.[29-33] As previously demonstrated by us, a planar quinoidal building block, *para*-azaquinodimethane (*p*-AQM), is easily accessible and has been successfully employed in organic semiconductors for OFETs and various applications.[34-40] The PA4T conjugated polymer, containing one *p*-AQM and one quaterthiophene in the repeat unit, exhibited superb crystallinity in both as-cast and annealed films.[40] However, only a mediocre hole mobility of 0.084 $cm^2 V^{-1} s^{-1}$ was obtained from PA4T-based OFETs, due to poor solubility and processibility arising from excessive interchain

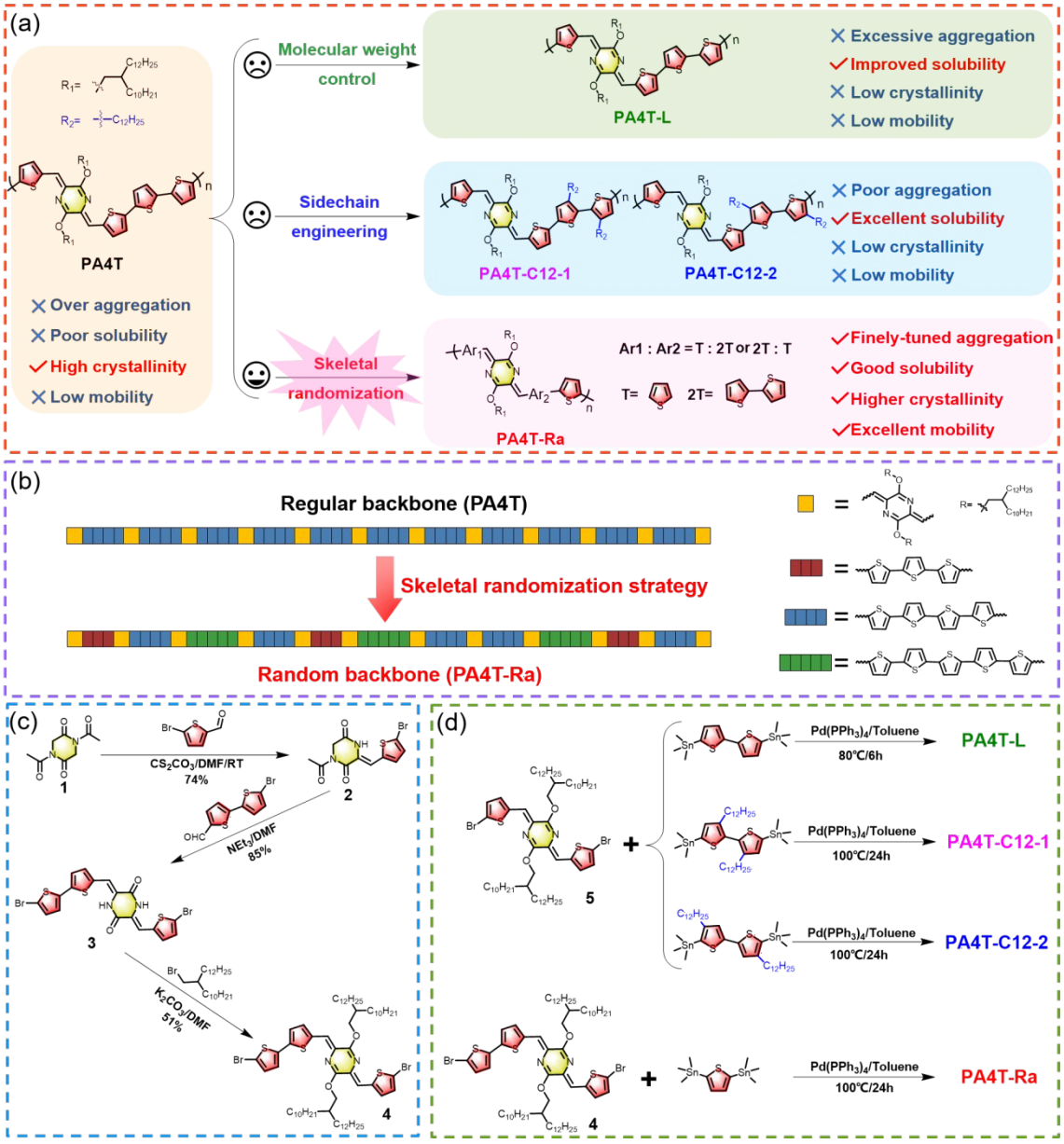


**Scheme 1**. a) Structures of the conjugated polymer PA4T and four PA4T homologues designed for comparative validation of the solubilization strategies. b) Schematic illustration of skeletal randomization strategy and backbone sequence of PA4T and PA4T-Ra. Synthetic routes to c) the dissymmetric dibromo-*p*-AQM-based monomer and d) the designed polymers.

interaction and high aggregation strength. Further effort of introducing longer side chains onto the backbone of PA4T showed limited improvement of solubility and hole mobility.[41] Given that PA4T represents a typical kind of quinoidal-aromatic CPs featuring a simple structure, strong aggregation and high film crystallinity, it serves as a great system to exercise novel strategies to address the solubility-performance dilemma.

Regioregularity control has recently emerged as a novel approach to construct high-performance D-A CPs, which has substantial impact on solubilities, backbone conformations,

interchain interactions, solid state microstructures, and corresponding device performance.[42-48] Traditionally, regioregular D-A polymers tend to show higher mobilities and more ordered microstructures than its regiorandom counterpart.[49-51] Recent advances, however, have demonstrated that regiorandom D-A polymers could show impressive charge transport.[52, 53] Despite the performance improvement, there lacks a detailed study to properly address the structure-property-performance relationship. For instance, there are several cases where regiorandom polymers exhibit both high mobilities and decreased thin film crystallinity,[54-56] which contradicts to the general relationship that high crystallinity typically translates to high mobility. More often, previous studies mainly focused on electronic properties as a result of regioregularity control, while little effort has been devoted to understanding its influence on the solubility and crystallization behavior of CPs.[57, 58] Clearly, a systematic study of the randomization effect in a well-defined conjugated polymer system would help inform more rational molecular design strategies.

Herein, regioregularity control is pioneered in the *p*-AQM-based quinoidal-aromatic CP setting by converting the regular backbone of PA4T into the polymer PA4T-Ra with random *p*-AQM-oligothiophene sequences. This skeletal randomization strategy, which features remarkable synthetic and structural simplicity, is compared against two other commonly adapted solubilization methods, i.e., molecular weight control and sidechain engineering, in its capacity to tune solubility, aggregation strength, and thin film properties (**Scheme 1**a and 1b). The systematic studies of the five quinoidal PA4T homologues revealed unconventional insights into the structure-property-performance relationships of conjugated polymers. As a result, the skeletal randomization strategy has been validated as the most effective methods in balancing solubility, fine tuning the interchain aggregation strength, and achieving highest crystallinity in thin films, which have substantial influence on charge carrier transport properties. The corresponding air-processed OFET devices based on PA4T-Ra showed remarkable operational stability and reliable hole mobilities up to 3.11 $cm^2 V^{-1} s^{-1}$, reflecting a more than 30-fold enhancement over the parent PA4T.

## 2. Results and Discussion

### 2.1. Polymer synthesis

The synthetic routes to dissymmetric dibromo-*p*-AQM-based monomer **4** and its derived regiorandom polymer PA4T-Ra were depicted in Scheme 1c and 1d, respectively. The synthesis of three regioregular PA4T polymer homologues was also illustrated in Scheme 1d. Detailed procedures and characterization were provided in Supporting Information. The preparation of

monomer **4** was accomplished in three straightforward steps from readily available starting materials in a high overall yield. The 1:1 Knoevenagel condensation between 1,4-diacetyl-2,5-diketopiperazine **1** and 5-bromothiophene-2-carbaldehyde gave rise to the monobromide **2** in 74% yield. Another 1:1 Knoevenagel condensation of compound **2** with 5'-bromo-[2,2'-bithiophene]-5-carbaldehyde afforded the dibromide **3** in excellent yield. Subsequent alkylation afforded the dibromo AQM monomer **4**. The other dibromo monomer **5** was synthesized in a similar fashion following previously reported procedures.[40] All polymers were prepared via Stille-coupling polymerization between the *p*-AQM-based dibromides and distannylated-thiophene monomers, while the molecular weight variations were controlled by altering the reaction temperature and duration.[59, 60] For the PA4T polymer with a lower molecular weight, PA4T-L, the polymerization was carried out at 80 °C for 6 h, while for keeping the molecular weights of PA4T-Ra, PA4T-C12-1 and PA4T-C12-2 to be comparable with that of PA4T, all of the reactions were carried out at 100 °C for 24 h. PA4T-C12-1 and PA4T-C12-2 were fractionated using chloroform (CF) while PA4T-L and PA4T-Ra were extracted with chlorobenzene using Soxhlet extractor, and the respective molecular weights were determined using high temperature size exclusion chromatography (SEC) at 140 °C with 1,2,4-trichlorobenzene as the eluent. As shown in **Table 1,** the number-average molecular weight ($M_n$) of PA4T-L was 13.9 kDa, lower than that of the previously reported PA4T (26.4 kDa), which was in the similar range as the other three polymers (23.9-27.0 kDa). Additionally, thermogravimetric analysis (TGA) and differential scanning calorimetry (DSC) were carried out to probe the thermal properties of all five polymers. As shown in Figure S1, all polymers presented decent thermal stability with a decomposition temperature ($T_d$) at a 5% weight loss in the range of 361–382 °C, and exhibited no distinct phase transition in the temperature range from 25 to 250 °C. The random backbone sequence of PA4T-Ra was confirmed by FTIR spectroscopic analysis.[55] As shown in Figure S2, PA4T-Ra shared many similar characteristic peaks for most of the spectra with the regular PA4T, because they have same chemical composition and proportion of primary units in the backbone. However, the figerprint region around 1051 $cm^{-1}$, which corresponds to C–C skeletal vibrations between two adjacent aromatic units, was distinctly different. PA4T-Ra showed multiple and featureless peaks, indicative of various sequences of aromatic units existing in the resulting random backbone, which correlates well with the expected chemical structure of PA4T-Ra in Scheme 1.

**Table 1**. Summary of molecular weight, solubility, optical band gap and electrochemical properties of the polymers.

| Polymer | $M_n$[a)] [kDa] | PDI | Solubility[b)] [mg mL$^{-1}$] | Solution | | | Film | | | HOMO[d)] [eV] | LUMO[e)] [eV] |
|---|---|---|---|---|---|---|---|---|---|---|---|
| | | | | $\lambda_{max1}$ [nm] | $\lambda_{max2}$ [nm] | $E_g$[c)] [eV] | $\lambda_{max1}$ [nm] | $\lambda_{max2}$ [nm] | $E_g$[c)] [eV] | | |
| PA4T[f)] | 26.4 | 2.7 | 5.2 | 660 | 731 | 1.54 | 660 | 731 | 1.53 | –5.07 | –3.54 |
| PA4T-L | 13.9 | 1.5 | 8.4 | 651 | 720 | 1.57 | 655 | 724 | 1.51 | –5.10 | –3.59 |
| PA4T-C12-1 | 27.0 | 2.3 | 53.1 | 590 | 672 | 1.72 | 563 | 603 | 1.67 | –5.23 | –3.56 |
| PA4T-C12-2 | 23.9 | 2.9 | 50.5 | 601 | – | 1.69 | 664 | 739 | 1.53 | –5.09 | –3.56 |
| PA4T-Ra | 25.1 | 2.4 | 17.8 | 667 | 731 | 1.56 | 667 | 734 | 1.50 | –5.03 | –3.53 |

[a)]Molecular weight by high temperature SEC. [b)]In chlorobenzene at 80 °C. [c)]Optical bandgaps estimated on the basis of the absorption onset. [d)]Measured by cyclic voltammetry. [e)]Calculated by subtraction of film optical bandgap from HOMO level. [f)]Reported previously.

### 2.2. Solubility test

The solubility of polymers is critical for achieving excellent charge carrier mobility, which has a dramatic influence on film formation, morphology and microstructure. Solubility tests were carried out to study the effectiveness of each solubility-tuning approach outlined in Scheme 1a. The previously reported polymer PA4T was insoluble in CB at room temperature (RT) and partially soluble in hot (80 °C) CB, while PA4T-L was solubilized more easily in CB. In addition, PA4T-C12-1 and PA4T-C12-2 were readily soluble in both CB and chloroform (CF) at RT, however PA4T-Ra was only partially soluble in RT CB (Figure S3, Supporting Information). Such observations indicated that solubilities of all four polymers were improved over PA4T. For quantitative comparison, the respective solubility limits for each polymer in 80 °C CB were determined using UV-vis absorption (Figure S4, Supporting Information) and summarized in Figure 1a and Table 1.[61, 62]

The solubilities of those polymers follow the trend of PA4T-C12-1 ≈ PA4T-C12-2 > PA4T-Ra > PA4T-L > PA4T. The trend indicates that attaching more sidechains to the polymer backbone results in excellent solubilities of up to above 50.5 mg mL$^{-1}$, while decreasing molecular weight of polymer works less effectively, resulting in limited improvement of the solubility (8.4 mg mL$^{-1}$). In addition, skeletal randomization transpires to a better solubility of 17.8 mg mL$^{-1}$ in the resulting polymer PA4T-Ra, which is twice of that of PA4T and sufficient for facile solution-based film formation. Among the three solubilization strategies, the skeletal randomization is more effective than controlling the molecular weight and less than introducing more solubilizing side chains. As shown in the following sections, this medium solubility

endowed the resulting polymer with sufficient processability and desirable aggregation in CB, allowing the fabrication of high mobility OFET devices.

### 2.3. Optoelectronic properties and aggregation behavior

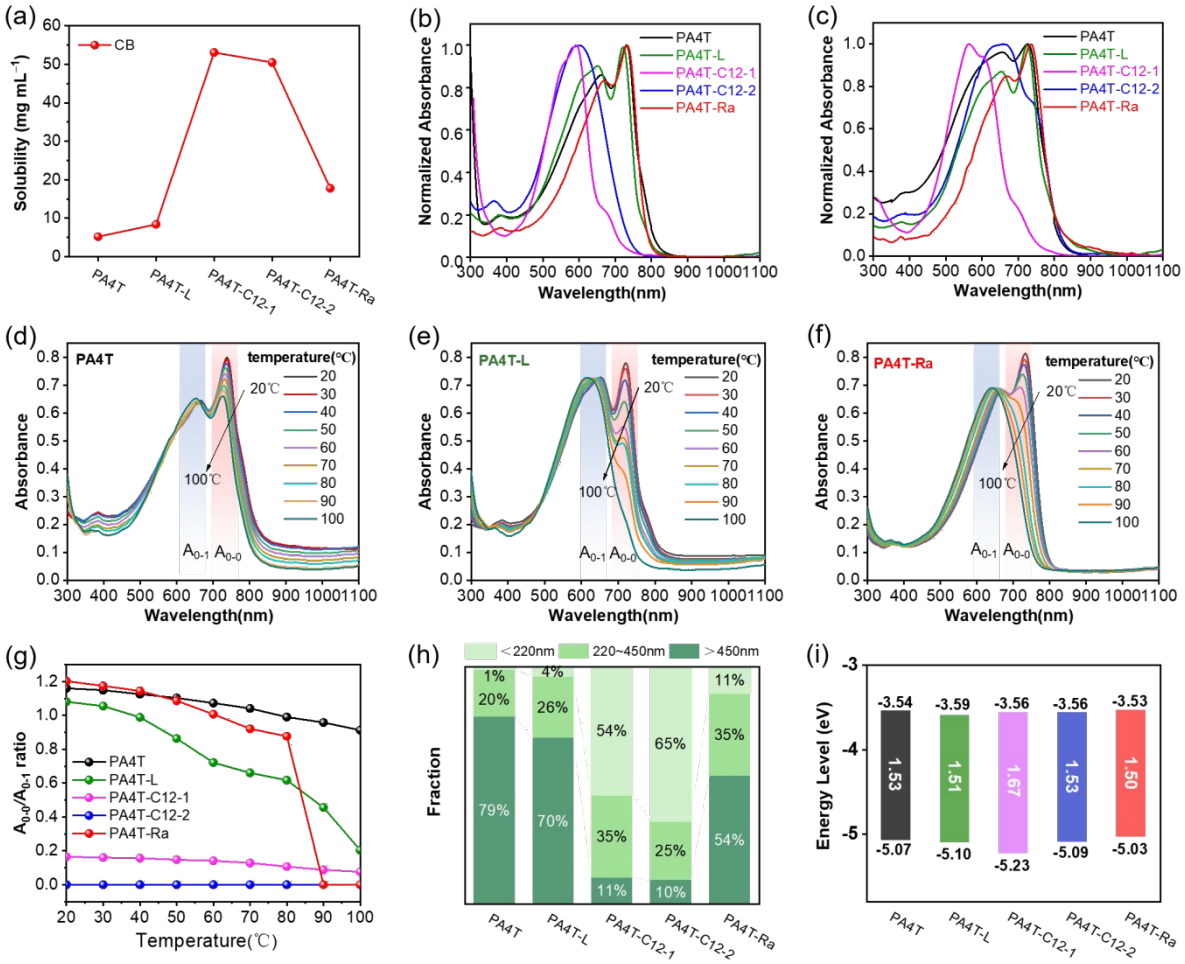


**Figure 1.** a) The solubilities of five polymers in 80 °C chlorobenzene. Normalized UV-vis absorption spectra of five polymers b) in chlorobenzene and c) thin film at room temperature. d-f) The evolution of UV-vis absorption spectra of PA4T, PA4T-L and PA4T-Ra in chlorobenzene during heating process. g) $A_{0-0}/A_{0-1}$ ratio of five polymers extracted from varied temperature UV-vis absorption spectra. h) Size distributions of solution aggregates at room temperature and i) diagram of energy levels of five polymers.

The UV-vis absorption spectra of all the PA4T polymers in dilute CB at RT and thin films are depicted in Figure 1b and 1c, respectively, and summarized in Table 1. In CB, PA4T-L with lower molecular weight displayed a similar but slightly blue-shifted absorption to that of PA4T, a result of decreased effective conjugation length as previously reported.[63] In the case of PA4T-C12-1 and PA4T-C12-2, substantial blue shift of the absorption maxima of around 100 nm was

observed when compared to that of PA4T, implying that the polymer backbones became more twisted after attaching two additional octyl sidechains to the repeat unit. Such conformational differences consequently led to weaker interchain interactions in PA4T-C12-1 and PA4T-C12-2 and corroborated their improved solubilities. In contrast, PA4T-Ra shared almost identical absorption behavior to PA4T, suggesting that randomization of the backbone imposed little influence on the chain coplanarity or interchain packing. Moreover, distinct 0−0 and 0−1 peaks were observed in the solution spectra of PA4T-L, PA4T-Ra and PA4T, indicating strong interchain aggregation in polymer solutions.[64, 65] The ratios of the peak intensities, $A_{0-0}/A_{0-1}$, were in the order of PA4T-Ra > PA4T > PA4T-L. As reported previously,[66, 67] a high $A_{0-0}/A_{0-1}$ ratio of above 1 corresponds to more ordered interchain packing. The highest $A_{0-0}/A_{0-1}$ ratio revealed a somewhat counterintuitive result that instead of disrupting the interchain packing, skeletal randomization reenforced such interactions and promoted the formation of more ordered aggregates. On the contrary, the absence of the obvious double-peak feature in the spectra of PA4T-C12-1 and PA4T-C12-2 suggested that the two solubility-tuning motifs severely disrupted the degree of interchain ordering in solution. When moving from solution to thin film, PA4T-C12-2 showed a pronounced red shift in its absorption while only slight spectrum broadening was observed for PA4T-C12-1, indicating significant enhancement of chain stacking for PA4T-C12-2 in the solid state. In clear contrast, the absorption features of PA4T-L, PA4T-Ra and PA4T were almost identical to their respective solution spectra, implying that strong pre-aggregated states have been established in solutions and remained after drying. Moreover, a similar trend in $A_{0-0}/A_{0-1}$ ratios was observed in thin films, where PA4T-Ra retained the highest $A_{0-0}/A_{0-1}$ ratio among all the polymers, correlating to its highest degree of order in interchain packing in solid state. To gain further insight into the relative strength of interchain aggregation in solution, which is decisive to the quality and morphology of corresponding thin-films, temperature-dependent absorption spectra of those polymers in CB were acquired. As shown in Figure 1d-f, Figure S5, Supporting Information, upon heating the solutions from 20 to 100 °C, 0−1 peaks of all polymers were progressively blue-shifted and the intensity of 0−0 peaks gradually decreased because of the enhanced backbone torsion and reduced effective conjugation length at higher temperature. For PA4T, a distinct 0−0 peak at ~726 nm was still retained with high $A_{0-0}/A_{0-1}$ ratio even at 100 °C, which implied the persistence of ultra-strong interchain aggregates that were in accordance with its high film roughness (see later sections). PA4T-L with lower molecular weight exhibited obviously diminished 0−0 peak, though the shoulder peak at ~720 nm remained distinguishable at even 100 °C with a greatly reduced $A_{0-0}/A_{0-1}$ ratio. In contrast, PA4T-Ra displayed the largest

variation of $A_{0-0}/A_{0-1}$ ratio across the temperature window, with the 0−0 peak disappearing at ~90 °C (Figure 1g). The highest temperature responsiveness for PA4T-Ra indicated that PA4T-Ra is more adaptive than PA4T and PA4T-L for assembly and reorganization towards ordered microstructures.[65] To gain quantitative insight into interchain aggregates in solution, filtration experiments were conducted to quantify the aggregate size of different polymers.[68-70] As shown in Figure 1h and Figure S6, Supporting Information, these PA4T polymers possessed distinctly varied size distributions of solution aggregates. The amounts of large aggregates (diameter > 450 nm) follow the trend of PA4T > PA4T-L > PA4T-Ra > PA4T-C12-1 > PA4T-C12-2, while small aggregates (diameter < 220 nm) are in the order of PA4T < PA4T-L < PA4T-Ra < PA4T-C12-1 < PA4T-C12-2. The above results evidence that the order of intermolecular interactions and the "relative aggregation strength" of those polymers is PA4T > PA4T-L > PA4T-Ra > PA4T-C12-1 > PA4T-C12-2, illustrating the impressive effectiveness of skeletal randomization in fine-tuning interchain aggregation with modest strength and high degree of structural order.

With the exception of PA4T-C12-1 of which the absorption edge was located at ~742 nm, all other polymers showed similar absorption edges of ~810 nm. The optical band gap ($E_g$) estimated from the film absorption edge is ~1.67 eV for PA4T-C12-1 and ~1.52 eV for the rest of other polymers. Cyclic voltammetry (CV) was carried out to estimate the energy levels of the PA4T-based polymers. The highest occupied molecular orbital (HOMO) energy levels were determined by the oxidation onsets while the lowest unoccupied molecular orbital (LUMO) levels were calculated from the HOMO level and corresponding optical band gap. As shown in Figure 1i and Figure S7, Supporting Information, and Table 1, all polymers showed comparable LUMO levels of around –3.55 eV and HOMO levels of around –5.05 eV, with the exception of PA4T-C12-1 which exhibited a lower HOMO level of –5.23 eV as a result of decreased coplanarity (see discussions below).

### 2.4. Theoretical calculations

In general, high backbone coplanarity can enhance intermolecular interactions, induce dense interchain packing and benefit charge carrier transport.[71] To gain a deeper understanding of the difference of interchain aggregation strength and illustrate the backbone conformation of those polymers, density functional theory (DFT) calculations employing B3LYP/ 6-311G (d,p) basis set were conducted based on a tetramer segment of each of the polymers.[36] For simplicity, sidechains were substituted with methyl groups in all segments. It is to be noticed that except

for PA4T-Ra, the donor moiety between two adjacent *p*-AQM units in the polymer backbone is quaterthiophene (4T), while PA4T-Ra comprises terthiophene (3T), 4T and

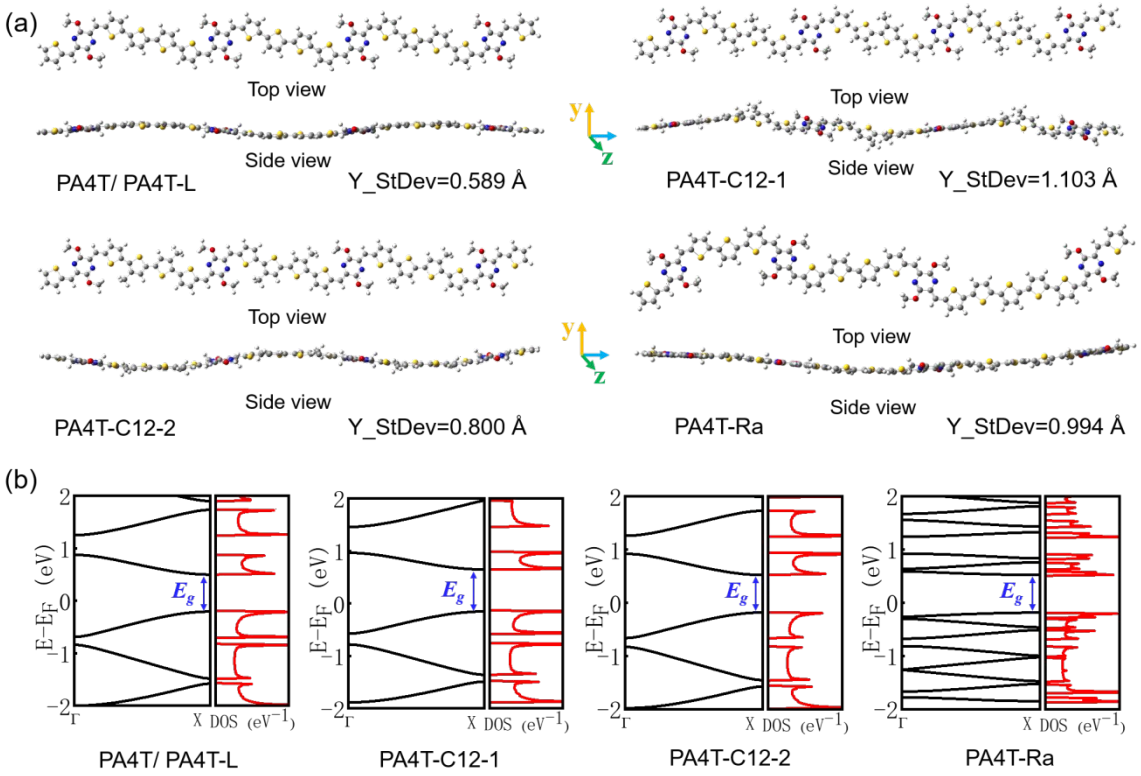


**Figure 2.** a) Optimized geometries and standard deviations of each atom in Y coordinates for the tetramer segments of PA4T homologues, where sidechains are replaced by methyl groups for simplicity. b) Band structures and partial densities of states (DOS) of PA4T homologues.

quinquethiophene (5T) as its donor moiety owing to the dissymmetric design. Here, one of the possible bonding modes involving all three oligothiophenes was modelled to represent the tetramer segment of PA4T-Ra. For comparison, the coplanarity of each segment of the polymers was quantified by the calculated standard deviation of atoms in Y coordinates (denoted as Y_StDev).[50] As depicted in Figure 2a, the Y_StDev for PA4T/PA4T-L, PA4T-C12-1, PA4T-C12-2 and PA4T-Ra was 0.589, 1.103, 0.800 and 0.994 Å, respectively. It can be seen that, except for PA4T-C12-2, the coplanarity of the rest of other polymers followed the order of PA4T/PA4T-L > PA4T-Ra > PA4T-C12-1, in good agreement with the above-mentioned trend of intermolecular interaction and "relative aggregation strength" in those polymers. However, in the case of PA4T-C12-2, despite its moderate coplanarity, the large steric hindrance and relatively large lamellar *d*-spacing (vide infra) caused by high density of sidechains in the backbone may give rise to weak interchain aggregation strength. Moreover, intrachain charge transport of those polymers was evaluated by the theoretical calculations of

effective hole masses ($m_h$*) utilizing Vienna *ab initio* simulation package (VASP) with the Perdew-Burke-Ernzerhof (PBE) functional.[72, 73] Band structures, partial densities of states (DOS) and calculated $m_h$* of polymers were illustrated in Figure 2b and Figure S8, Supporting Information. The theoretically predicted band gaps of those polymers were in the approximate order of PA4T-C12-1 > PA4T/PA4T-L ≈ PA4T-C12-2 ≈ PA4T-Ra, consistent with the experiment results. Moreover, PA4T/PA4T-L, PA4T-C12-1 and PA4T-C12-2 had a comparable $m_h$* in the range of 0.143 to 0.169 $m_e$, while considerably smaller $m_h$* of 0.115 $m_e$ was obtained for PA4T-Ra. The smallest $m_h$* for PA4T-Ra is presumably originated from its smallest degree of bond length alternation (BLA) among all the polymers (Figure S9), which is consistent with previous report.[74] The small $m_h$* implies efficient intrachain hole transport along the backbone of PA4T-Ra,[74] which correlates well with its remarkably high hole mobility achieved in PA4T-Ra based OFET device (vide infra).

## 2.5. Thin film microstructures and morphologies

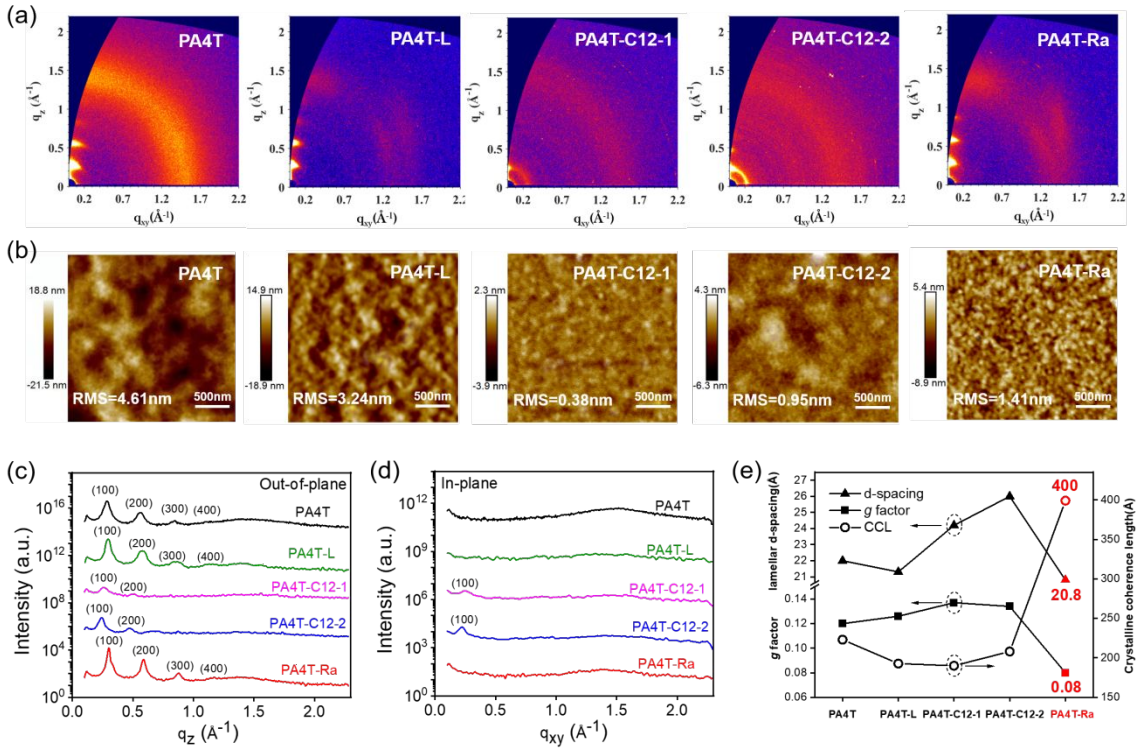


**Figure 3.** a) GIWAXS patterns and b) AFM topography images of five annealed polymer films. Line-cut profiles along c) out-of-plane and d) in-plane directions for five annealed polymer films. d) Comparison of lamellar d-spacing, crystalline coherence length, and g factor of five annealed polymer films.

Solution-state aggregation behavior has critical influence on solid-state microstructures and morphologies of CPs.[75] To gain insight into the morphological properties of these polymer films, grazing-incidence wide-angle X-ray scattering (GIWAXS) measurement and tapping-mode atomic force microscopic (AFM) characterization were performed (Figure 3 and Figure S10, Supporting Information). As previously reported, PA4T exhibited obvious (h00) diffraction peaks (h up to 4) and a feeble (010) diffraction in the out-of-plane (OOP) direction with a lamellar d-spacing of 22.0 Å, indicating a predominant edge-on orientation. The spectrum of PA4T-L showed similar OOP diffraction peaks albeit with weaker intensity, suggesting its slighter lower crystallinity. In the case of PA4T-C12-1 and PA4T-C12-2, not only the OOP diffraction peak intensity was greatly diminished, commensurate with the disappearance of higher order (300) and (400) peaks, but also the (100) diffraction in the in-plane (IP) direction showed up, which indicated a bimodal texture due to the emergence of face-on oriented crystallites. The lamellar d-spacings of PA4T-C12-1 and PA4T-C12-2 increased to 24.2 and 26.0 Å, respectively, in accordance with the less dense packing due to the additional octyl sidechains attached to the polymer backbone. As for PA4T-Ra, the diffraction pattern was similar to that of PA4T while the peak intensity was higher and a smaller lamellar distance of 20.8 Å was observed, indicative of better crystallinity, tighter chain packing and the preservation of edge-on orientation preference in the random polymer. Crystalline coherence lengths (CCL) and paracrystalline disorder (*g* factor), which represent the crystalline domain size and packing dislocation, respectively, were calculated to quantitatively compare the crystallinity and degree of crystalline perfectness in those polymers.[76, 77] As shown in Figure 3e and summarized in **Table 2,** all polymers except PA4T-Ra exhibited a small CCL in the range of 190-223 Å and large paracrystalline disorder in the range of 12.1-13.7%, corresponding to relatively lower film crystallinity and higher structural disorder in the solid state. In sharp contrast, fine tuning the aggregation to medium strength via skeletal randomization resulted in a significantly larger CCL of 400 Å and a lower paracrystalline disorder of 8.1% in the thin film of PA4T-Ra, corresponding to a highly ordered packing structure desirable for better charge carrier transport in OFET devices. It should be noted that there is no (010) diffraction in the IP direction for all the polymer films, a peak that is typically expected from π–π stacking in lamellar conjugated polymers. Instead, the scattering signal in the shape of a concentrated arc at q ~1.6 $Å^{-1}$ at azimuth angle of ~30°, as observed in the GIWAXS spectra of PA4T-L and PA4T-Ra (Figure 3a), is presumably originated from π-π stacking. The atypical location of the π-π stacking peak, which is unique to AQM and oligothiophene-based conjugated polymers, is ascribed to the formation of a structure that is distinct from the commonly observed

orthorhombic structure in crystalline conjugated polymers.[21] The exact structure however remains unassigned and requires future in-depth study.

**Table 2**. Summary of GIWAXS data of annealed thin films of polymers.

| Polymer | Lamellar d-spacing[a)] (Å) | CCL[b)] (Å) | *g* factor[b)] (%) |
|---|---|---|---|
| PA4T | 20.5[c] | 223 | 12.1 |
| PA4T-L | 21.3 | 193 | 12.6 |
| PA4T-C12-1 | 24.2 | 190 | 13.7 |
| PA4T-C12-2 | 26.0 | 208 | 13.4 |
| PA4T-Ra | 20.8 | 400 | 8.1 |

[a)] Lamellar d-spacing ware calculated according to OOP (100) diffraction peaks. [b)] Crystalline coherence length and *g* factor were calculated according to OOP (200) diffraction peaks. [c)]Reported previously.

In addition, the as-cast films of those polymers showed decreased crystallinity compared to their annealed films, concomitant with smaller RMS surface roughness of as-cast films as seen in AFM images (Figure S11, Supporting Information). In comparison to PA4T, the four new polymers exhibited surface roughness in the range of 0.38-3.24 nm, lower than that of PA4T (4.61 nm). The surface roughness of those five polymers followed the order of PA4T > PA4T-L > PA4T-Ra > PA4T-C12-2 > PA4T-C12-1, in close agreement with the trends in aggregation strengths and solubilities. In particular, discontinuous and large domains of aggregates were observed in both PA4T and PA4T-L films. On the other hand, PA4T-C12-1 and PA4T-C12-2 films displayed featureless and smooth surface morphologies with RMS roughness of below 1 nm. In contrast, the annealed film of PA4T-Ra showed an appropriate RMS value of 1.4 nm and interconnected grains. The uniform surface and formation of interconnected network is expected to favor charge carrier transport across crystalline grain boundaries.

It is generally believed that strong interchain aggregation would be advantageous to realize high crystallinity and ordered packing in CPs.[78] Nevertheless, the relative crystallinity observed in those five polymers, in the order of PA4T-Ra > PA4T > PA4T-L > PA4T-C12-1 ≈ PA4T-C12-2, is inconsistent with their "relative aggregation strength" which follows the order of PA4T > PA4T-L > PA4T-Ra > PA4T-C12-1 > PA4T-C12-2. A plausible transition from solution aggregates to thin-film microstructures was outlined in **Figure 4** to enlighten the

seemingly contradictory results whereas PA4T-Ra with modest aggregation strength could deliver unusually high crystallinity and ordered structure.

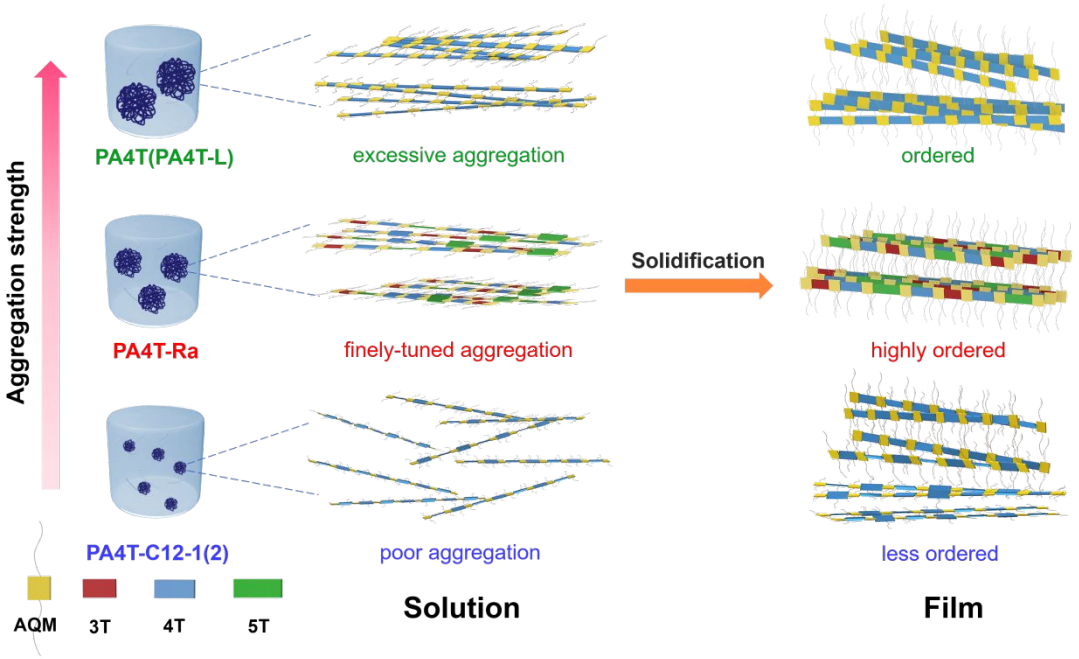


**Figure 4**. Schematic illustration of the proposed transitions from solution aggregates to thin-film microstructures for polymers with different aggregation strength.

While lowering the molecular weight of PA4T improves the solubility and slightly modulates its aggregation strength, both PA4T and PA4T-L displayed excessive aggregation in solution. The overly strong interchain interactions and intensively tight chain entanglements may limit the polymers' ability to reorganize and reassemble into more ordered packing during film-forming process. On the other hand, the conventional solubilization strategy of introducing alkyl chains was too disruptive to interchain interactions, resulting in much reduced aggregation strength and poorly ordered structures in the thin film. Notably, the skeletal randomization strategy stands out as a counterintuitive method that endows a goldilocks zone for the aggregation strength in solution, which facilitates self-assembly of polymer chains into orderly packed structures in highly crystalline films. Such correlations are consistent with previous findings by Pei and coworkers who have demonstrated that solution-state aggregation critically determines solid-state microstructures and corresponding charge transport.[69]

In order to get in-depth understanding of the counterintuitive result, we further included a regioregular polymer PA3T, containing one *p*-AQM and one terthiophene (3T) in the repeat unit, in the comparisons against PA4T and PA4T-Ra. Polymer PA3T comprising the smaller-sized terthiophene moiety was reported by us previously as an analogue to PA4T.[38, 40] It exhibits reduced solution-state aggregation strength in comparison with PA4T, which is comparable to

that of PA4T-Ra (Figure S12). However, $A_{0-0}/A_{0-1}$ ratios in RT solution and thin film are both below 1, implying less ordered interchain packing in PA3T. This can be attributed to the increased side chain density and the upraised steric hindrance effect in PA3T when compared to PA4T and PA4T-Ra, endowing an improved solubility of 23.1 mg $mL^{-1}$ for PA3T (Table S1).[79] Compared to PA4T, PA3T film shows a larger lamellar d-spacing of 22.3 Å, a smaller CCL of 205 Å and a higher *g* factor of 12.8%, while PA4T-Ra delivers a larger CCL of 400 and a smaller *g* factor of 8.1% (Table S1). Consequently, PA3T and PA4T-Ra analogues share comparable solution-state aggregation strength but possess distinctly different film crystallinity and lattice disorder. We accordingly propose that the difference in film microstructures may be related to the density and distribution of side chains in polymer backbone. Despite that moderate aggregation strength is favorable for the reorganization and reassembly of polymer chains into more ordered packing during solidification, the increased side chain density in PA3T would impede interchain interaction and packing, resulting in decreased crystallinity and increased lattice disorder. Randomizing the backbone sequence can not only give rise to moderate aggregation strength, but also maintain the average side chain density along the PA4T-Ra backbone because of distributed arrangement of side chains. Such arrangement would not impede dense interchain packing in film, but can instead facilitate more ordered packing owing to the favorable interchain interactions. On the other hand, the presence of longer quinquethiophene (5T) segment in PA4T-Ra compared to 4T and 3T may facilitate adjacent interchain contact, which also possibly contributes to the dense interchain packing during solidification and/or interchain charge transport.[80] Overall, the two factors, namely moderate aggregation strength and the distributed arrangement of side chains, together account for the optimal solid-state microstructure and efficient charge transport observed in PA4T-Ra (vide infra).

### 2.6. OFET Fabrication and Characterization

OFET devices with a bottom-gate top-contact (BGTC) configuration were fabricated using chlorinated solvents (a mixture of CB and CF) to investigate the charge transport properties of those CPs. Both the deposition of active layers and the measurement of OFET characteristics were conducted in ambient environment, a condition that is desirable for low-cost processing and scale-up. Representative transfer and output characteristics were shown in **Figure 5**a and 5b, and Figure S13, Supporting Information, and device performance was summarized in Figure S14, Supporting Information, and **Table 3** and Table S2, Supporting Information. Despite the

improved solubility for PA4T-L, PA4T-C12-1 and PA4T-C12-2, they showed only modest hole mobilities in the range of 0.041 to 0.062 $cm^2\ V^{-1}\ s^{-1}$. The mobilities were slightly lower than

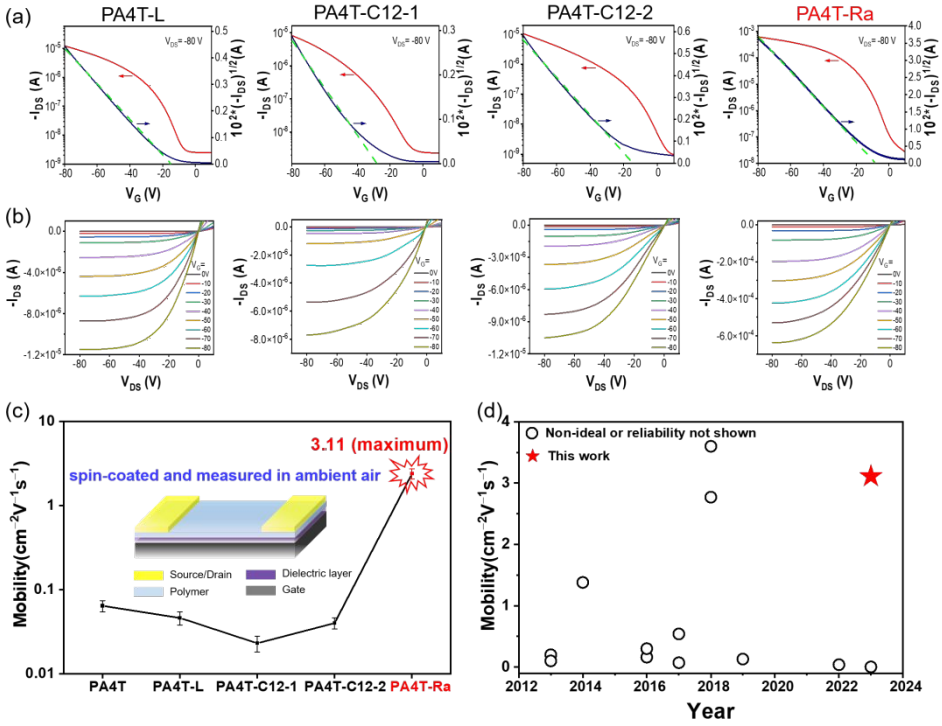


**Figure 5.** Typical a) transfer and b) output characteristics of annealed OFETs based on four new polymers using chlorinated solvents. c) Comparison of maximum hole mobilities of the PA4T homologues. d) Hole mobilities of OFETs based on quinoid-donor polymers characterized by conventional spin-coating deposition method in recent 10 years.

**Table 3**. OFET performances, reliability factor and effective hole masses of the polymers.

| Polymer | $\mu_{h,\,max}$ [$\mu_{h,\,avg}$][a)] [$cm^2\ V^{-1}\ s^{-1}$] | $V_{th}$ [V] | $I_{on/off}$ | $\gamma$[b)] [%] | $m_h^*(m_e)$[c)] |
|---|---|---|---|---|---|
| PA4T[d)] | 0.084 (0.082±0.003) | –5 | $10^4$-$10^5$ | —[e)] | 0.149 |
| PA4T-L | 0.062 (0.046 ± 0.008) | –14 | $10^2$-$10^3$ | 97.1 | 0.149 |
| PA4T-C12-1 | 0.041 (0.023 ± 0.005) | –17 | $10^3$-$10^4$ | 66.6 | 0.169 |
| PA4T-C12-2 | 0.059 (0.040 ± 0.006) | –16 | $10^4$-$10^5$ | 79.6 | 0.143 |
| PA4T-Ra | 3.11 (2.39 ± 0.33) | –10 | $10^3$-$10^4$ | 88.3 | 0.115 |

[a)]Maximum mobility under optimized annealing conditions, Average mobilities were calculated based on 10 independent devices and listed in parentheses. [b)]Reliability factor γ calculated according to ref [77-78]. [c)]Effective hole mass ($m_h$*) extracted from the theoretical calculations. $m_e$ represents the mass of an electron. [d)]Reported previously. [e)]Not available.

that of PA4T and correlated well with the polymers' relatively small CCL and large paracrystalline disorder. It is worth noting that alkylated bithiophene with head-to-head (HH) linkage tend to have a large dihedral angle, endowing the resulting polymer with twisted backbone, amorphous film morphology and poor charge carrier mobility according to previous literature.[25] Lower carrier mobility is expected for the HH linkage-based PA4T-C12-1 than the non-alkylated bithiophene-based PA4T and tail-to-tail (TT) linkage-based PA4T-C12-2. While this is the case, the observed mobilities are in the same order and essentially comparable, suggesting that there are other contributing factors to the hole transporting properties, for instance, surface roughness and lamellar d-spacings. Impressively, PA4T-Ra delivered an excellent hole mobility of up to 3.11 $cm^2 V^{-1} s^{-1}$, which is more than 30-times higher than that of PA4T and 50-times higher than that of other three polymers (Figure 5c). Moreover, the device behavior was characterized by a high reliability coefficient of 88%.[81, 82] This mobility, to the best of our knowledge, is among the highest for quinoidal-donor polymer-based, spuncast OFETs with a satisfying reliability factor (Figure 5d**,** Figure S15 and Table S3, Supporting Information). Additionally, the dependence of mobilities on gate voltages was studied for all four polymers to further evaluate the validity of the extracted mobility. As shown in Figure S16, PA4T-L and PA4T-Ra-based OFET devices showed a low gate voltage dependence (i.e., small mobility variations) in the range of −30 to −80 V, while in the case of PA4T-C12-1 and PA4T-C12-2, low gate voltage dependence was only observed in a narrower range between −60 and −80 V. Such contrast in gate voltage dependence is in accordance with the high reliability factors observed in PA4T-L and PA4T-Ra based devices. To evaluate the batch-to-batch reproducibility of the resulting polymer based on skeletal randomization strategy, a second batch of polymer was prepared under the same polymerization condition, which also exhibited similar charge transport properties with hole mobility of 2.98 $cm^2 V^{-1} s^{-1}$ (Figure S17 and Table S4). The results confirmed that skeletal randomization could be able to impart the resulting random polymer with highly reproducible properties, which is essential for large-scale synthesis.

The use of chlorinated solvents during the fabrication of high mobility OFET device has been a source of health and environmental concerns, which demands the substitution of ecofriendly non-chlorinated solvents, such as THF for ambient-processed OFETs. Given that non-chlorinated and non-aromatic tetrahydrofuran (THF) is structurally distinct from chlorobenzene (CB) used in our original manuscript, we have selected ecofriendly THF as the solvent and systematically investigated the solubility, solution aggregation, film morphology and hole mobility of PA4T-Ra and its homologous polymers. As shown in Figure S18a, the solubilities

of the PA4T, PA4T-L, PA4T-C12-1, PA4T-C12-2 and PA4T-Ra are 2.3, 4.5, 50.2, 48.9 and 10.2 mg $mL^{-1}$ in THF, respectively, which are much lower than their respective solubility in CB because of the weaker dissolving capability of THF and follow the same trend of PA4T-C12-1 ≈ PA4T-C12-2 > PA4T-Ra > PA4T-L > PA4T. In addition, all five polymers processed in THF exhibited similar absorption features as those processed in CB, except that $A_{0-0}/A_{0-1}$ ratios in THF-deposited films were slightly lower than those obtained from CB, which indicated that solid-state interchain packing become less ordered when processed from THF (Figure S18b and c). The variable temperature UV-vis absorption spectra of all five polymers in THF (from 20 to 60 °C) are shown in Figure S18d-h, which demonstrate that the order of "relative aggregation strength" of the polymers roughly follow the trend of that in CB. Moreover, OFET devices based on these THF-processed polymers are also fabricated and measured in ambient air. As presented in Figure S19 and summarized in Table S5, those OFET devices exhibited similar *p*-type transport behavior as those fabricated using chlorinated solvents. Impressively, PA4T-Ra delivers a hole mobility of up to 0.83 $cm^2\ V^{-1}\ s^{-1}$, representing one of the first examples on quinoidal CP-based OFETs processed from a non-chlorinated solvent. Despite the lower mobility than that obtained from CB, the mobility of PA4T-Ra remains to rank the highest amongst the five polymers, underscoring the effectiveness of skeletal randomization strategy in constructing high-performing non-chlorinated solvent-processed conjugated polymers. Thin film morphology and microstructure of PA4T-Ra deposited from THF are further studied to correlate with its hole transport properties (Figure S20). Sharp (h00) (h is up to 4) diffraction peaks, together with a weak (010) diffraction peak in the OOP direction and the lack of obvious IP patterns in annealed PA4T-Ra, indicate the presence of predominant edge-on oriented crystallites similar to those from CB. Moreover, the calculated CCL was as large as 356 Å while the *g* factor was only 9.2%, supporting the high crystallinity of the film.

### 2.7. OFET Device Stability

Operational stability under bias and storage stability in ambient air are essential for practical usage and future commercialization of OFETs, thus it is important to evaluate such characteristics of those AQM polymers. As depicted in **Figure 6**a, after applying $V_G$ of −80 and 0 V at $V_{DS}$ of −80 V up to 9000 cycles (4000 s), PA4T and PA4T-L exhibited fluctuant on-current and off-current, showing a certain degree of operational instability. For PA4T-C12-1 and PA4T-C12-2 with low crystallinity, the operational instability became more pronounced, as characterized by larger fluctuations in on-current and off-current and obviously eroded on/off

ratio. In contrast, impressive operational stability was observed for PA4T-Ra, of which the on/off currents and ratios remained nearly constant. The relative operational stability of the five

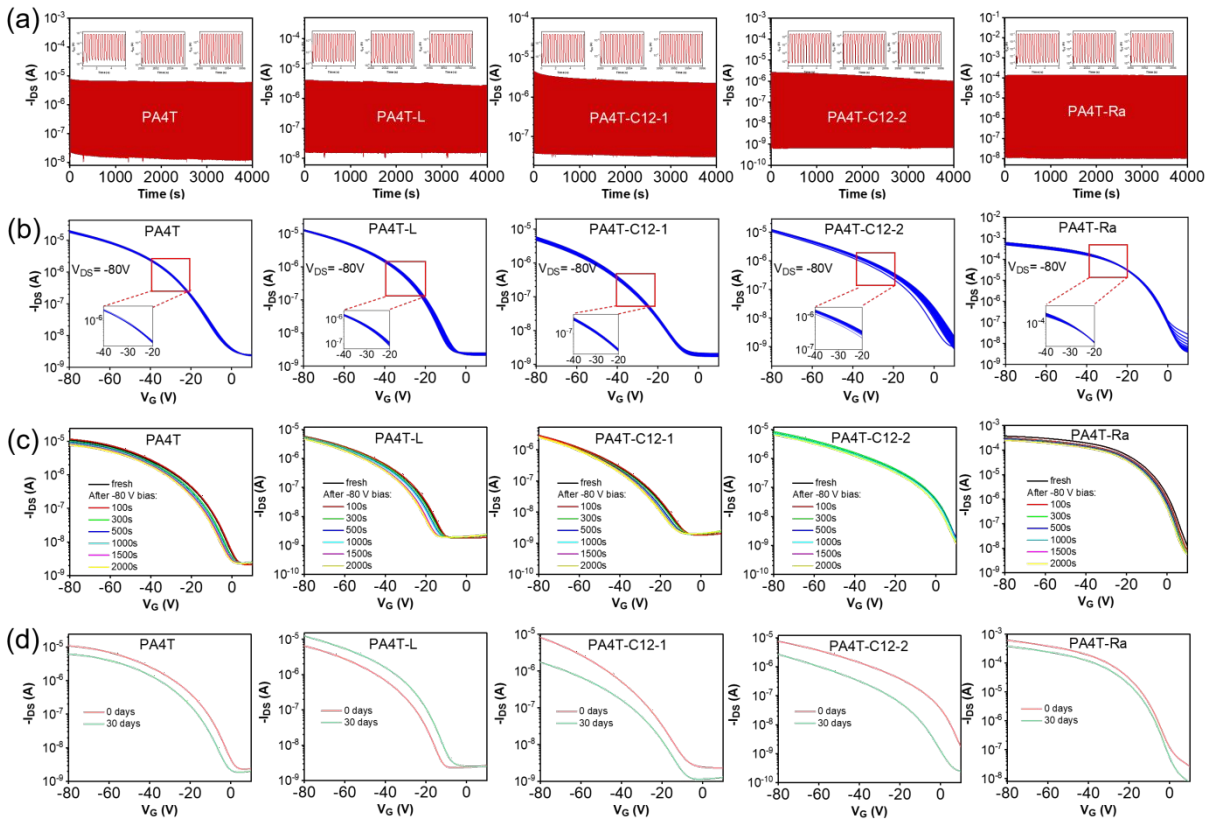


**Figure 6.** a) On-off cycle tests (9000 cycles) on OFET devices by applying $V_G$ of −80 and 0 V at $V_{DS}$ of −80 V. b) Repeatability of series of transfer curves (30 cycles) of OFET devices at $V_{DS}$ of −80 V. c) Bias stress tests on OFET devices by applying prolonged bias voltage of −80 V for up to 2000 s. d) Transfer curves of OFET devices before and after storing in ambient air for 30 days.

polymers correlated well with their film crystallinity and structural disorder, i.e., polymers with higher crystallinity and less structural disorder delivered greater operational stability. Further repeatability of transfer characteristics and bias stress stability were also studied, again revealing trends that were consistent with the relative operational stability and the film crystallinity (Figure 6b and c). Additionally, transfer characteristics of OFET devices based on those polymers were measured before and after storing in ambient air at a relative humidity of 56% for 30 days to reveal their storage stabilities (Figure 6d). Among these results, PA4T-Ra-based devices displayed the slightest shift of its transfer characteristics, attesting to the best storage stability for PA4T-Ra. Overall, PA4T-Ra with the highest crystallinity and least

structural disorder exhibits the best operational and environmental stabilities, a trend that is consistent with previous reports.[36, 83]

## 3. Conclusion

In summary, a skeletal randomization strategy was introduced as a potent tool to tune the solubility and aggregation strength of quinoid-aromatic CPs for better charge transport in OFET devices. Various homologues of CPs with the same overall backbone composition were designed and synthesized according to three solubilization strategies, allowing for a comparative and systematic study to validate the effectiveness of this strategy. The influence of molecular structures on solubility, aggregation behavior, optoelectronic properties, film morphologies, microstructures and OFET performance were thoroughly investigated. Despite the disparity in the effectiveness in improving solubilities, more significant distinctions were observed in their interchain aggregation behavior in solution and thin film crystallinities. Remarkably, random polymer PA4T-Ra accessed by the facile skeletal randomization strategy exhibited modest aggregation strength, giving rise to largest crystalline coherence length and lowest structural disorder in the film. Consequently, OFET devices based on PA4T-Ra displayed excellent hole mobilities up to 3.11 $cm^2 V^{-1} s^{-1}$, amounting to more than 30 times improvement over the other PA4T homologues. Future investigation of temperature effect on polymer aggregation and film microstructures is desired for further optimization of charge transport properties. The PA4T-Ra represents a rare and counterintuitive example where "disorder" introduced along the main chain of conjugated polymers has dramatically improved the film crystallinity and enhanced the charge carrier mobility, with the added benefit of improved solution processibility, and excellent operational and air stability of the resulting devices. Theoretical insights revealed that PA4T-Ra has the smallest effective hole mass among all the PA4T homologues, corroborating with efficient intrachain hole transport. This study, for the first time, offers a fresh perspective on the use of skeletal randomization to enhance film crystallinity of CPs. We expect that the underutilized skeletal randomization strategy can be implemented more generally in developing practical, high-performing CPs, potentially accelerating the large-scale manufacturing of superior organic electronic devices.

## Author contributions

Quanfeng Zhou: Conceptualization, Data curation, Formal analysis, Methodology, Writing–original draft. Jinlun Li: Data curation, Formal analysis, Visualization, Writing–original draft. Cheng Liu: Data curation, Formal analysis, Methodology, Software, Writing–original draft.

Runze Xie: Data curation, Methodology, Software. Guoxiang Zhang: Data curation, Formal analysis, Software. Xiang Ge: Data curation, Formal analysis. Zesheng Zhang: Data curation, Formal analysis. Lianjie Zhang: Data curation, Resources. Junwu Chen: Data curation, Formal analysis, Resources. Xiu Gong, Data curation, Formal analysis, Resources. Chen Yang: Resources, Software. Yuanyu Wang: Data curation, Formal analysis, Funding acquisition, Resources, Software, Writing–review&editing. Yi Liu: Conceptualization, Funding acquisition, Methodology, Supervision, Writing–review&editing. Xuncheng Liu: Conceptualization, Formal analysis, Funding acquisition, Project administration, Supervision, Writing–original draft.

**Conflicts of interest**

The authors declare that they have no known competing financial interests or personal relationships that could have appeared to influence the work reported in this paper.

**Corresponding authors**

*Xuncheng Liu: xcliu3@gzu.edu.cn

*Yi Liu: yliu@lbl.gov

*Yuanyu Wang: yuanyuwang0216@163.com

**Acknowledgements**

This work was supported by Nature Science Foundation of Guizhou Provincial Science and Technology Department (QKHJC ZK [2021] general 247), Natural Science Research Young Talents Project of Provincial Education Department (No. Guizhou Education & KY word [2022] 105), the National Natural Science Foundation of China (52363021, 22305050). Part of the work was performed as a user project at the Molecular Foundry, a national user facility supported by the Office of Science, Office of Basic Energy Sciences, of the U.S. Department of Energy under Contract No. DE-AC02-05CH11231. The authors thanks for the computing support of the State Key Laboratory of Public Big Data at Guizhou University.

**Electronic supplementary information (ESI)**

Supplementary data to this article can be found online.

**References**

1. M. Luo, L. Kong, J. Liang, Z. Zhang, S. Deng, L. Zhang, X. Qiao, D. Ma and J. Chen, *Chem. Eng. J.*, 2023, **457**, 141281.
2. R. Ma, K. Zhou, Y. Sun, T. Liu, Y. Kan, Y. Xiao, T. A. Dela Peña, Y. Li, X. Zou, Z. Xing, Z. Luo, K. S. Wong, X. Lu, L. Ye, H. Yan and K. Gao, *Matter*, 2022, **5**, 725-734.
3. X. Liu, L. Nian, K. Gao, L. Zhang, L. Qing, Z. Wang, L. Ying, Z. Xie, Y. Ma, Y. Cao, F. Liu and J. Chen, *J. Mater. Chem. A*, 2017, **5**, 17619-17631.
4. X. Cao, H. Li, J. Hu, H. Tian, Y. Han, B. Meng, J. Liu and L. Wang, *Angew. Chem. Int. Ed.*, 2023, **62**, e202212979.
5. J. Meng, J. Dou, Z. Zhou, P. Chen, N. Luo, Y. Li, L. Luo, F. He, H. Geng, X. Shao, H.-L. Zhang and Z. Liu, *Angew. Chem. Int. Ed.*, 2023, **62**, e202301863.
6. J. Chen, W. Zhang, L. Wang and G. Yu, *Adv. Mater.*, 2023, **35**, 2210772.
7. Y. Shi, J. Li, H. Sun, Y. Li, Y. Wang, Z. Wu, S. Y. Jeong, H. Y. Woo, S. Fabiano and X. Guo, *Angew. Chem. Int. Ed.*, 2022, **61**, e202214192.
8. C. Gao, A. Shukla, H. Gao, Z. Miao, Y. Zhang, P. Wang, G. Luo, Y. Zeng, W. W. H. Wong, T. A. Smith, S.-C. Lo, W. Hu, E. B. Namdas and H. Dong, *Adv. Mater.*, 2023, **35**, 2208389.
9. C. Dong, S. Deng, B. Meng, J. Liu and L. Wang, *Angew. Chem. Int. Ed.*, 2021, **60**, 16184-16190.
10. A. Nawaz, L. Merces, L. M. M. Ferro, P. Sonar and C. C. B. Bufon, *Adv. Mater.*, 2023, **35**, 2204804.
11. Q. Zhang, T. Jin, X. Ye, D. Geng, W. Chen and W. Hu, *Adv. Funct. Mater.*, 2021, **31**, 2106151.
12. Y. Woo, W. Hong, S. Y. Yang, H. J. Kim, J.-H. Cha, J. E. Lee, K. J. Lee, T. Kang and S.-Y. Choi, *Adv. Electron. Mater.*, 2018, **4**, 1800251.
13. Q. Liu, Y. Wang, A. Kohara, H. Matsumoto, S. Manzhos, K. Feron, S. E. Bottle, J. Bell, T. Michinobu and P. Sonar, *Adv. Funct. Mater.*, 2020, **30**, 1907452.
14. C. Grand, W. Zajaczkowski, N. Deb, C. K. Lo, J. L. Hernandez, D. G. Bucknall, K. M üllen, W. Pisula and J. R. Reynolds, *ACS Appl. Mater. Interfaces*, 2017, **9**, 13357-13368.
15. I. Osaka, M. Saito, H. Mori, T. Koganezawa and K. Takimiya, *Adv. Mater.*, 2012, **24**, 425-430.
16. S. Lv, L. Li, Y. Mu and X. Wan, *Polym. Rev.*, 2021, **61**, 520-552.
17. J. Mei and Z. Bao, *Chem. Mater.*, 2014, **26**, 604-615.
18. T. Lei, J.-Y. Wang and J. Pei, *Chem. Mater.*, 2014, **26**, 594-603.
19. Q. Chen, Y. H. Han, L. R. Franco, C. F. N. Marchiori, Z. Genene, C. M. Araujo, J.-W. Lee, T. N.-L. Phan, J. Wu, D. Yu, D. J. Kim, T.-S. Kim, L. Hou, B. J. Kim and E. Wang, *Nano-Micro Lett.*, 2022, **14**, 164.
20. Y. Yang, Z. Liu, G. Zhang, X. Zhang and D. Zhang, *Adv. Mater.*, 2019, **31**, 1903104.
21. I. Osaka and K. Takimiya, *Polymer*, 2015, **59**, A1-A15.
22. A. Zen, J. Pflaum, S. Hirschmann, W. Zhuang, F. Jaiser, U. Asawapirom, J. P. Rabe, U. Scherf and D. Neher, *Adv. Funct. Mater.*, 2004, **14**, 757-764.
23. Y. Ding, Y. Zhu, X. Wang, Y. Wang, S. Zhang, G. Zhang, X. Gu and L. Qiu, *Chem. Mater.*, 2022, **34**, 2696-2707.
24. Y. Ran, Q. Li, J. Li, Y. Sun, W. Shi, Y. Guo and Y. Liu, *Adv. Electron. Mater.*, 2021, **7**, 2100526.
25. K. Yang, Z. Chen, Y. Wang and X. Guo, *Acc. Mater. Res.*, 2023, **4**, 237-250.
26. M. Li, Z. Li, D. Yu, M. Wang, D. Wang and B. Wang, *Chem. Eur. J.*, 2023, **29**, e202202930.
27. J. Huang and G. Yu, *Mater. Chem. Front.*, 2021, **5**, 76-96.
28. X. Ji and L. Fang, *Polym. Chem.*, 2021, **12**, 1347-1361.
29. Y. Choi, Y. Kim, Y. Moon, I.-B. Kim, H. Hwang and D.-Y. Kim, *J. Mater. Chem. C*, 2022, **10**, 17874-17885.

30. M. Yang, T. Du, X. Zhao, X. Huang, L. Pan, S. Pang, H. Tang, Z. Peng, L. Ye, Y. Deng, S. Mingliang, C. Duan, H. Fei and C. Yong, *Sci. China: Chem.*, 2021, **64**, 1219-1227.
31. T. Mikie and I. Osaka, *J. Mater. Chem. C*, 2020, **8**, 14262-14288.
32. Y. Kim, H. Hwang, N.-K. Kim, K. Hwang, J.-J. Park, G.-I. Shin and D.-Y. Kim, *Adv. Mater.*, 2018, **30**, 1706557.
33. K. Kawabata, M. Saito, I. Osaka and K. Takimiya, *J. Am. Chem. Soc.*, 2016, **138**, 7725-7732.
34. X. Liu, C. L. Anderson and Y. Liu, *Acc. Chem. Res.*, 2023, **56**, 1669-1682.
35. C. L. Anderson, T. Zhang, M. Qi, Z. Chen, C. Yang, S. J. Teat, N. S. Settineri, E. A. Dailing, A. Garzón-Ruiz, A. Navarro, Y. Lv and Y. Liu, *J. Am. Chem. Soc.*, 2023, **145**, 5474-5485.
36. H. Liang, C. Liu, Z. Zhang, X. Liu, Q. Zhou, G. Zheng, X. Gong, L. Xie, C. Yang, L. Zhang, B. He, J. Chen and Y. Liu, *Adv. Funct. Mater.*, 2022, **32**, 2201903.
37. C. L. Anderson, H. Li, C. G. Jones, S. J. Teat, N. S. Settineri, E. A. Dailing, J. Liang, H. Mao, C. Yang, L. M. Klivansky, X. Li, J. A. Reimer, H. M. Nelson and Y. Liu, *Nat. Commun.*, 2021, **12**, 6818.
38. C. Liu, X. Liu, G. Zheng, X. Gong, C. Yang, H. Liu, L. Zhang, C. L. Anderson, B. He, L. Xie, R. Zheng, H. Liang, Q. Zhou, Z. Zhang, J. Chen and Y. Liu, *J. Mater. Chem. A*, 2021, **9**, 23497-23505.
39. C. L. Anderson, N. Dai, S. J. Teat, B. He, S. Wang and Y. Liu, *Angew. Chem. Int. Ed.*, 2019, **58**, 17978-17985.
40. X. Liu, B. He, C. L. Anderson, J. Kang, T. Chen, J. Chen, S. Feng, L. Zhang, M. A. Kolaczkowski, S. J. Teat, M. A. Brady, C. Zhu, L.-W. Wang, J. Chen and Y. Liu, *J. Am. Chem. Soc.*, 2017, **139**, 8355-8363.
41. X. Liu, B. He, A. Garzon-Ruiz, A. Navarro, T. L. Chen, M. A. Kolaczkowski, S. Feng, L. Zhang, C. A. Anderson, J. Chen and Y. Liu, *Adv. Funct. Mater.*, 2018, **28**, 201801874.
42. Y. Kim, H. Park, J. S. Park, J.-W. Lee, F. S. Kim, H. J. Kim and B. J. Kim, *J. Mater. Chem. A*, 2022, **10**, 2672-2696.
43. J.-W. Lee, C. Sun, S.-W. Lee, G.-U. Kim, S. Li, C. Wang, T.-S. Kim, Y.-H. Kim and B. J. Kim, *Energy Environ. Sci.*, 2022, **15**, 4672-4685.
44. P. J. Leenaers, H. van Eersel, J. Li, M. M. Wienk and R. A. J. Janssen, *Macromolecules*, 2020, **53**, 7749-7758.
45. S. W. Kim, H. Kim, J.-W. Lee, C. Lee, B. Lim, J. Lee, Y. Lee and B. J. Kim, *Macromolecules*, 2019, **52**, 738-746.
46. E. L. Melenbrink, K. M. Hilby, M. A. Alkhadra, S. Samal, D. J. Lipomi and B. C. Thompson, *ACS Appl. Mater. Interfaces*, 2018, **10**, 32426-32434.
47. J. B. Howard and B. C. Thompson, *Macromol. Chem. Phys.*, 2017, **218**, 1700255.
48. H. H. Choi, J. Y. Baek, E. Song, B. Kang, K. Cho, S.-K. Kwon and Y.-H. Kim, *Adv. Mater.*, 2015, **27**, 3626-3631.
49. L. Ying, F. Huang and G. C. Bazan, *Nat. Commun.*, 2017, **8**, 14047.
50. J. Yuan, M. J. Ford, Y. Zhang, H. Dong, Z. Li, Y. Li, T.-Q. Nguyen, G. C. Bazan and W. Ma, *Chem. Mater.*, 2017, **29**, 1758-1768.
51. H. Zhong, C.-Z. Li, J. Carpenter, H. Ade and A. K. Y. Jen, *J. Am. Chem. Soc.*, 2015, **137**, 7616-7619.
52. J. Lee, S. H. Kang, S. M. Lee, K. C. Lee, H. Yang, Y. Cho, D. Han, Y. F. Li, B. H. Lee and C. Yang, *Angew. Chem. Int. Ed.*, 2018, **57**, 13629-13634.
53. K. H. Park, S. Y. Son, J. O. Kim, G. Kang, T. Park and D. Kim, *J. Phys. Chem. Lett.*, 2018, **9**, 3173-3180.
54. S. Y. Son, K. Choi, J. Lee, H. I. Kim, T. Park and M. Kim, *Chem. Mater.*, 2022, **34**, 4856-4864.

55. C. Zhou, Z. Chen, G. Zhang, C. McDowell, P. Luo, X. Jia, M. J. Ford, M. Wang, G. C. Bazan, F. Huang and Y. Cao, *Adv. Energy Mater.*, 2018, **8**, 1701668.
56. S. Y. Son, J. W. Kim, J. Lee, G.-W. Kim, J. Hong, J. Y. Kim and T. Park, *J. Mater. Chem. A*, 2018, **6**, 24580-24587.
57. J. Ji, X. Wu, P. Deng, D. Zhou, D. Lai, H. Zhan and H. Chen, *J. Mater. Chem. C*, 2019, **7**, 10860-10867.
58. Y. Ji, C. Xiao, Q. Wang, J. Zhang, C. Li, Y. Wu, Z. Wei, X. Zhan, W. Hu, Z. Wang, R. A. J. Janssen and W. Li, *Adv. Mater.*, 2016, **28**, 943-950.
59. Z. Wang, M. Gao, C. He, W. Shi, Y. Deng, Y. Han, L. Ye and Y. Geng, *Adv. Mater.*, 2022, **34**, 2108255.
60. X. Yuan, Y. Zhao, T. Zhan, J. Oh, J. Zhou, J. Li, X. Wang, Z. Wang, S. Pang, P. Cai, C. Yang, Z. He, Z. Xie, C. Duan, F. Huang and Y. Cao, *Energy Environ. Sci.*, 2021, **14**, 5530-5540.
61. Z. Wang, X. Song, Y. Jiang, J. Zhang, X. Yu, Y. Deng, Y. Han, W. Hu and Y. Geng, *Adv. Sci.*, 2019, **6**, 1902412.
62. L. Ye, W. Li, X. Guo, M. Zhang and H. Ade, *Chem. Mater.*, 2019, **31**, 6568-6577.
63. T. J. Fauvell, T. Zheng, N. E. Jackson, M. A. Ratner, L. Yu and L. X. Chen, *Chem. Mater.*, 2016, **28**, 2814-2822.
64. Z. Chen, P. Cai, J. Chen, X. Liu, L. Zhang, L. Lan, J. Peng, Y. Ma and Y. Cao, *Adv. Mater.*, 2014, **26**, 2586-2591.
65. H. Hu, P. C. Y. Chow, G. Zhang, T. Ma, J. Liu, G. Yang and H. Yan, *Acc. Chem. Res.*, 2017, **50**, 2519-2528.
66. J. Ma, Z. Liu, J. Yao, Z. Wang, G. Zhang, X. Zhang and D. Zhang, *Macromolecules*, 2018, **51**, 6003-6010.
67. S. H. Yu, K. H. Park, Y.-H. Kim, D. S. Chung and S.-K. Kwon, *Macromolecules*, 2017, **50**, 4227-4234.
68. M. Li, H. Bin, X. Jiao, M. M. Wienk, H. Yan and R. A. J. Janssen, *Angew. Chem. Int. Ed.*, 2020, **59**, 846-852.
69. Z.-F. Yao, Z.-Y. Wang, H.-T. Wu, Y. Lu, Q.-Y. Li, L. Zou, J.-Y. Wang and J. Pei, *Angew. Chem. Int. Ed.*, 2020, **59**, 17467-17471.
70. H.-L. Yi and C.-C. Hua, *Macromolecules*, 2019, **52**, 332-340.
71. W. Zhang, K. Shi, J. Lai, Y. Zhou, X. Wei, Q. Che, J. Wei, L. Wang and G. Yu, *Adv. Mater.*, 2023, **35**, 2300145.
72. C. Cheng, H. Geng, Y. Yi and Z. Shuai, *J. Mater. Chem. C*, 2017, **5**, 3247-3253.
73. J. Yang, Z. Zhao, H. Geng, C. Cheng, J. Chen, Y. Sun, L. Shi, Y. Yi, Z. Shuai, Y. Guo, S. Wang and Y. Liu, *Adv. Mater.*, 2017, **29**, 201702115.
74. T. Mikie, M. Hayakawa, K. Okamoto, K. Iguchi, S. Yashiro, T. Koganezawa, M. Sumiya, H. Ishii, S. Yamaguchi, A. Fukazawa and I. Osaka, *Chem. Mater.*, 2021, **33**, 8183-8193.
75. Z.-F. Yao, J.-Y. Wang and J. Pei, *Prog. Polym. Sci.*, 2023, **136**, 101626.
76. J. Rivnay, S. C. B. Mannsfeld, C. E. Miller, A. Salleo and M. F. Toney, *Chem. Rev.*, 2012, **112**, 5488-5519.
77. J. Rivnay, R. Noriega, R. J. Kline, A. Salleo and M. F. Toney, *Phys. Rev. B*, 2011, **84**, 045203.
78. R. Noriega, J. Rivnay, K. Vandewal, F. P. V. Koch, N. Stingelin, P. Smith, M. F. Toney and A. Salleo, *Nat. Mater.*, 2013, **12**, 1038-1044.
79. R. Zhao, C. Dou, Z. Xie, J. Liu and L. Wang, *Angew. Chem. Int. Ed.*, 2016, **55**, 5313-5317.
80. R. Stalder, S. R. Puniredd, M. R. Hansen, U. Koldemir, C. Grand, W. Zajaczkowski, K. Müllen, W. Pisula and J. R. Reynolds, *Chem. Mater.*, 2016, **28**, 1286-1297.

81. Y. Xu, Y. Li, S. Li, F. Balestra, G. Ghibaudo, W. Li, Y.-F. Lin, H. Sun, J. Wan, X. Wang, Y. Guo, Y. Shi and Y.-Y. Noh, *Adv. Funct. Mater.*, 2020, **30**, 1904508.
82. H. H. Choi, K. Cho, C. D. Frisbie, H. Sirringhaus and V. Podzorov, *Nat. Mater.*, 2018, **17**, 2-7.
83. W. H. Lee, H. H. Choi, D. H. Kim and K. Cho, *Adv. Mater.*, 2014, **26**, 1660-1680.